



On the Mechanism Responsible for Extreme Turbulence Intensity Generation in the *Hi-Pilot* Burner

Isaac G. Boxx¹ · Aaron W. Skiba² · Campbell D. Carter² · Alberto Ceschin³ · Francisco E. Hernández Pérez³ · Hong G. Im³

Received: 26 October 2021 / Accepted: 22 March 2022 / Published online: 21 April 2022
© The Author(s) 2022

Abstract

In this study, we apply particle image velocimetry (PIV), hot-wire anemometry (HWA), and large-eddy simulation (LES) to identify and characterize a key mechanism by which high-intensity turbulence measured in the “*Hi-Pilot*” burner is generated. Large-scale oscillation of the high-velocity jet core about its own mean axial centerline is identified as a dominant feature of the turbulent flow field produced by this piloted Bunsen burner. This oscillation is linked to unsteady flow separation along the expanding section of the reactant nozzle and appears stochastic in nature. It occurs over a range of frequencies (100–300 Hz) well below where the turbulent kinetic energy (TKE) spectrum begins to follow a $-5/3$ power law and results in a flow with significant scale separation in the TKE spectrum. Although scale separation and intermittency are not unusual in turbulent flows, this insight should inform analysis and interpretation of previous, and future studies of this unique test case.

Keywords Hi-Pilot burner · Premixed flames · Extreme turbulence intensity · Flamelet · Jet oscillation

1 Introduction

The structure and dynamics of a turbulent flame depend strongly on two coupled non-dimensional parameters: the turbulence Reynolds number (Re_t) and the Karlovitz number (Ka), defined as

$$Re_t = \frac{u' \delta}{\nu} \quad (1)$$

✉ Isaac G. Boxx
isaac.boxx@dlr.de

¹ German Aerospace Center (DLR), 70569 Stuttgart, Germany

² Air Force Research Laboratory, Wright-Patterson Air Force Base, Ohio 45433, USA

³ King Abdullah University of Science and Technology (KAUST), CCRC, Thuwal 23955-6900, Saudi Arabia

$$Ka = \left(\frac{u'}{s_l} \right)^{3/2} \left(\frac{l_f}{s_l} \right)^{1/2} \quad (2)$$

where u' is the root-mean-square (RMS) of velocity fluctuations of the flow, δ is the flow integral length scale, ν is the kinematic viscosity of the reactants, l_f is the flame thickness and s_l is the laminar flame speed of the reactants. Re_t represents the ratio of inertial and viscous forces in a turbulent fluid, and is a key determinant of mixing and shear characteristics. Ka represents the ratio of the chemical- and the Kolmogorov timescales of a turbulent flame. The strong coupling of Re_t and Ka , combined with pressure-dependence of ν, s_l and l_f pose a major challenge when it comes to the modelling of flames at elevated pressure.

Turbulent flames are frequently modelled according to the flamelet assumption (Driscoll 2008; Peters 2000; Janicka and Sadiki 2005). According to this model (Peters 1986), chemical reactions in a turbulent flame occur in 1D layers (or “flamelets”) that are sufficiently thin to escape penetration by even the smallest scale turbulent eddies in the flow and whose thermochemical structure, therefore, mimics that of a laminar flame. The effect of turbulence under these conditions is to wrinkle and stretch this layer, generating or eliminating flame surface area in the process. This approach has the advantage of enabling modelers to separate the effects of turbulence and chemistry and thereby simplify numerical simulations. Unfortunately, a key assumption of the flamelet model, i.e. that the flamelet is sufficiently thin to escape penetration by small-scale turbulent eddies, may break down at conditions of extreme turbulence intensity.

Large-scale gas turbine (GT) power plants typically operate at pressures in excess 20 bars, have u' values of several tens of m/s and relatively large integral scales (1 cm or more) in the combustor. This results in flame conditions with both very high Re_t and high Ka . According to classical combustion theory (Driscoll 2008; Peters 2000; Janicka and Sadiki 2005), this pushes flames in GT combustors toward the “thickened flamelet / distributed reactions” regime. In the thickened flamelet regime, the flamelet is no longer thin enough to escape penetration by turbulent eddies in the flow, with the result that the flame pre-heat layer is broadened by turbulent mixing. In the distributed reactions regime, it is theorized that heat-release reactions cease to occur in discrete layers altogether, rendering the separation of fluid-dynamics and chemistry in combustion models impossible. A survey of recent experimental studies, however, failed to find evidence of broadened reaction zones at the conditions theorized (Skiba et al. 2018). A numerical study by Weller et al., (Weller et al. 1998) did find evidence of distributed combustion in a premixed hydrogen-air flame at conditions of extreme turbulence intensity ($Re_t=4442$), but only at a Karlovitz number considerably higher ($Ka=8767$) than one may expect in a gas turbine combustor.

To understand the structure and dynamics of turbulent flames in the thickened flamelet and distributed reactions regime, there is no substitute for detailed experimental measurements acquired in flames at these conditions. To reach these conditions at atmospheric pressure is, however, highly challenging, requiring either complex turbulence generation schemes (Skiba et al. 2018, 2021; Wabel et al. 2017, 2018), or very high velocities and considerable piloting and/or dilution (Li et al. 2014; Zhou et al. 2014, 2015a, b, 2017a, b; Wang et al. 2019). A much more challenging alternative is to maintain low to moderate velocities and turbulence intensities, and increase the chamber pressure to match the thermochemical properties found in a practical combustion device (Griebel et al. 2007; Venkateswaran et al. 2014). To date, the overwhelming majority of experimental studies on premixed flames subject to extreme turbulence intensities have focused on flames at atmospheric pressure (Driscoll et al. 2020).

The “Hi-Pilot” burner (Skiba et al. 2018, 2021; Wabel et al. 2017, 2018), designed at the University of Michigan, is a piloted, premixed Bunsen burner designed to reach the extreme Karlovitz number conditions necessary to rigorously explore the existence and limits of the theoretical “distributed combustion” regime at atmospheric pressure conditions. The Hi-Pilot is one of only a few burners able to reach these conditions at atmospheric pressure and has been the focus of numerous experimental and theoretical studies in recent years. As shown in Table S1 in the Supplemental Material, there have been at least 20 peer-reviewed journal papers published on this burner to date, including four major review articles the past two years alone. The median number of citations received by these papers (since 2016) is 14, with the seven most referenced having been cited between 39 and 85 times each. Despite the strong interest this burner has received from the combustion community, to date no study has rigorously identified the mechanism by which it generates the extreme turbulence intensities it is reported to produce. This complicates both the interpretation and modelling of experimental data acquired in flames produced by this much studied burner. In this study, we seek to address this gap in the literature using both experimental and numerical techniques.

In the *Hi-Pilot* burner, reactants enter via a cylindrical plenum. The plenum is filled with glass beads to homogenize the flow. The reactants then pass a radially-slotted turbulence generator plate (with 70, 80 or 95% blockage ratio) into an axisymmetric converging–diverging nozzle. Whereas the converging section of the nozzle follows a polynomial profile, the expanding section is approximately linear. Additional reactants (6% of the total flow through burner) are injected at the throat of the converging–diverging nozzle. Reactants then exit the burner via a 21.6 mm diameter nozzle, where they burn under the stabilizing influence of a large (108-mm diameter) axisymmetric, premixed methane-air pilot flame.

The *Hi-Pilot* burner is shown schematically in Fig. 1. Based on laser Doppler anemometry (LDA) measurements, Wabel et al. (Wabel et al. 2017, 2018) and Skiba et al. (Skiba et al. 2021) report measuring flames with u'/U values of up to 47%, longitudinal integral scales of up to 41 mm and Re_t of up to 99,000 in this burner. The values reported in these studies are largely consistent with measurements acquired in premixed Bunsen burners that use a high blockage-ratio, radially slotted turbulence generator plate followed by a high contraction-ratio nozzle (Venkateswaran et al. 2011; Marshall et al. 2011). The turbulence intensities generated in the *Hi-Pilot* are certainly impressive

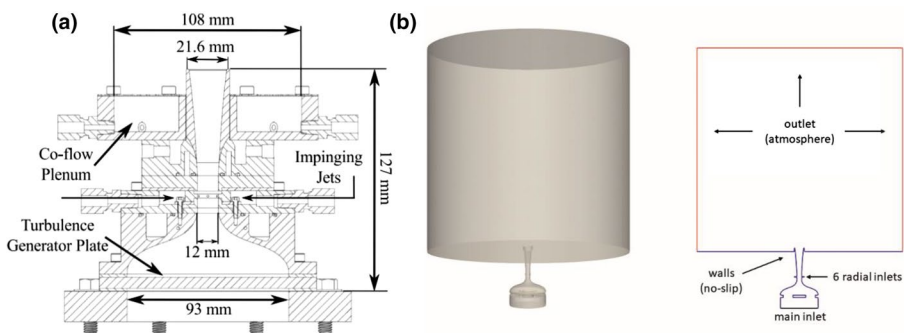


Fig. 1 a Schematic of the Hi Pilot Burner. Reproduced from (Peters 1986) with permission of the author. b Computational domain and boundary conditions at each outer surface

when compared to those generated by a conventional square mesh array (Roach 1986) or fractal (Hurst and Vassilicos 2007) grid. The same studies, however, also reveal issues that render the turbulent flow generated in the *Hi-Pilot* rather challenging to interpret and/or model.

The measurements presented in Wabel et al. (2017) and Skiba et al. (2018) report that the non-dimensional turbulence intensity (u'/U) measured in the burner for a given turbulence generator plate varies strongly with bulk flow velocity. For example, measurements on a flow using “Plate A”, which has a 70% blockage ratio, show that turbulence intensity varies from 22 to 47% as the bulk flow velocity is increased from 14 to 78 m/s. At the same time, the measured longitudinal integral scale is reported to vary from 7.5 to 41 mm. Given that the burner internal geometry remains the same across this increase in reactant velocity, these observations indicate the turbulent flow at the exit may not be fully developed or “mature”, and there may be significant separation between the larger, more energetic length scales and those that follow the classical $-5/3$ scaling relation for turbulent kinetic energy (TKE) spectra. If this is indeed the case, it would have significant implications for the modelling and simulation of flames in this burner. Given that the *Hi-Pilot* is being used to probe challenging and as-yet unexplored regions of the turbulent combustion regime diagram, it is essential to fully understand the nature of the turbulent flow it generates.

A possible explanation for the exceptionally high turbulence intensities measured in the *Hi-Pilot* is transient flow separation of the reactant jet in the nozzle. One may approximate the expanding section of the *Hi-Pilot* nozzle as an axisymmetric linear diffuser with a (2θ) expansion angle of 9 degrees, and L/d of approximately 4.1. Comparing this idealized approximation of the nozzle to the stability map for subsonic linear diffusers (Fox and Kline 1962), one sees that the internal geometry of the *Hi-Pilot* is likely susceptible to transient flow-separation. Transitory stall in a linear diffuser is known to induce a strongly unsteady flow (White 1998). Intermittency stemming from unsteady oscillation or “flapping” of the high-velocity core of the jet about the burner axial centerline would explain much of the measured turbulent flow characteristics reported in the *Hi-Pilot* burner. In particular, intermittency associated with the side-to-side oscillation of the high velocity core of the reactant jet about the burner axial centerline would manifest itself as a high measured turbulence intensity (u'/U) there. Furthermore, a side-to-side oscillation of the high velocity core of the reactant jet could easily dominate correlation statistics at the centerline. In this case, the measured integral timescale would be characteristic of the jet-oscillation frequency rather than a turbulent eddy turnover time and thereby explain how a burner with a 21.6 mm exit diameter has been measured to produce flows with an integral length scale of 41 mm. Finally, it would also explain the sensitivity of both u'/U and longitudinal integral scale to the bulk flow velocity, given that dynamics of transient flow separation in a diffuser is highly sensitive to this parameter.

The goal of this study is to identify and characterize the mechanism by which the *Hi-Pilot* burner achieves high turbulence intensities and longitudinal integral scales. To this end, particle image velocimetry (PIV) and hot-wire anemometry (HWA) are used to explore the non-reacting flow-field downstream of the burner exit, while high-fidelity large-eddy simulation (LES) is used to explore the in-nozzle flow. As the goal of the study is to understand the mechanism by which the burner generates the extreme turbulence intensities reported in previous studies, and the flow upstream of the burner exit consists of unburned reactants, only non-reacting flow is considered. In this way, we intend to enable more robust interpretation of data measured in this much-studied burner configuration.

2 Experimental Setup

2.1 Hi-Pilot Burner

The *Hi-Pilot* burner is shown schematically in Fig. 1a. Detailed descriptions of this burner can be found elsewhere (Driscoll 2008; Fox and Kline 1962; Griebel et al. 2007; Hurst and Vassilicos 2007), so only a brief review of its key attributes is provided here. This burner is best described as an axisymmetric converging–diverging nozzle with a contraction ratio of 7.8 and an expansion ratio of 1.8, where the exit diameter is 21.6 mm. In this study, a fixed, radially slotted plate with a blockage ratio of 80% was positioned just upstream of the contraction. This plate corresponds to the “B-plate” described in prior works (Driscoll 2008; Fox and Kline 1962; Griebel et al. 2007; Hurst and Vassilicos 2007). Six small holes (exit diameter of 1.3 mm) at the throat of the burner allowed fluid to be injected perpendicularly to the primary flow such that a jet-in-cross-flow configuration is formed. The combination of the turbulence generator plate, jets-in-cross-flow, and the converging–diverging nozzle have been shown in previous studies to yield a highly turbulent flow at the burner exit (Driscoll 2008; Fox and Kline 1962; Griebel et al. 2007; Hurst and Vassilicos 2007). Under reacting flow conditions, fuel and air are mixed upstream of the cylindrical plenum. The plenum is filled with glass beads in order to homogenize the flow before it encounters the turbulence plate. To stabilize a flame at the exit of the nozzle, a large-diameter (108 mm) pilot flame sits ≈ 10 mm below the exit plane of the nozzle. In the current study, only non-reacting conditions are considered.

2.2 Flow Condition

The *Hi-Pilot* burner was operated at non-reacting conditions designed to match those referred to in Skiba et al. (2018) as “Case 3B.” This was achieved by matching the total reactant flow rate (i.e., fuel plus air) in both the main nozzle and the turbulence generator jets with equivalent volumetric flow rates of air. Although this will slightly change the overall mixture density, due to the lower density of the fuel in the reacting flow case, this change is considered negligible for the purposes of this study.

The air for the main flow (577.6 g/min) was metered through an electromechanical mass flow controller (MFC) and monitored via a Coriolis flow meter (Siemens Sitrans DI-15). The air for the turbulence generator jets (36.9 g/min) was metered through a separate MFC and monitored via a Coriolis flow meter (Sitrans DI3). Approximately 20% of the air to the central nozzle was diverted through a fluidized bed particle seeder during measurements to ensure high seed density for the PIV measurements.

2.3 Particle Image Velocimetry

Two highspeed, 2-component particle image velocimetry (PIV) systems were used to acquire velocity field measurements in the plane parallel to the axial flow direction. Both PIV systems relied on the same dual-cavity, diode-pumped solid-state laser (Edgewave IS200-2-LD, ≈ 9 mJ/pulse, 7.5 ns pulse duration) for illumination. The output of the laser was formed into a collimated sheet of approximately 60 mm height via a cylindrical telescope and focused to a thin waist with a third cylindrical lens. The time separation between the pulses for each measurement was 10 μ s.

The first PIV system used a highspeed CMOS camera (LaVision HSS8) equipped with a 100-mm focal length, $f/2.8$ macro objective (Tokina) to image elastic scattering from titanium dioxide particles seeded into the flow. Seeding was accomplished via a fluidized bed particle seeder, and seed was injected into the air flow immediately upstream of the (glass bead filled) burner plenum. This PIV system was used to image the flow over a relatively large ($74 \times 61 \text{ mm}^2$) field of view (FOV). Velocity vectors were computed from the particle images using an adaptive multi-pass cross-correlation algorithm (LaVision Davis 10) with interrogation windows ranging from 64×64 to $32 \times 32 \text{ pixel}^2$, and 50% overlap, resulting in vector resolution and spacing of 1.53 and 0.77 mm, respectively. Single-shot measurement uncertainty (based on PIV correlation statistics) for this system is approximately 2.1 m/s at the jet centerline.

The second PIV system used a similar highspeed CMOS camera (LaVision HSS8), mounted on the opposite side of the laser sheet. The camera was equipped with a 200 mm focal length, $f/4$ macro objective (Nikon). This PIV system was used to image the flow within a smaller ($27 \times 21 \text{ mm}^2$) FOV and thus with a higher spatial resolution than achievable with the first system. Velocity vectors were computed from the particle images with interrogation windows ranging from 64×64 to $16 \times 16 \text{ pixel}^2$, and 50% overlap, resulting in vector resolution and spacing of 0.77 and 0.38 mm, respectively. Single-shot measurement uncertainty (based on PIV correlation statistics) for this system is approximately 2 m/s at the jet centerline. Each PIV system was used to acquire 10,000 dual-frame images per measurement run at 10 kHz, corresponding to 1 s of continuous measurement time. Two measurement runs were acquired for analysis in this study. As both PIV systems relied on the same laser for simultaneous illumination, the pulse separation time for both systems was identical.

2.4 Hotwire Anemometry

In addition to the PIV measurements, single-point velocity time-series measurements were acquired with a hotwire anemometer (Dantec Dynamics StreamLine 90CN10 operated with a 55P61 X-probe). The hotwire was calibrated for flow and direction both before and after the primary measurements via a designated calibration system (Dantec Dynamics StreamLine Pro Automatic Calibrator) over a range of angles and velocities ranging from 0.5 to 60 m/s, which encapsulates the expected velocities considered in this study. Fourth order polynomials were fit to both the pre- and post-calibration data and used to convert the measured voltages to velocities. Prior to this conversion, however, the velocities were corrected for local temperature variations via temperature measurements made with an integral probe. The velocity values produced by the pre- and post-calibrations were averaged together to yield the final result.

Hotwire measurements were made at 27 radial locations spaced by 1 mm at a distance of 5 mm downstream of the exit of the nozzle. The hotwire system was operated with a sampling rate of 100 kHz over a duration of 5 s. Thus, each measurement location consists of 500,000 instantaneous samples. Additionally, a low-pass filter with a 30 kHz cutoff was applied (via the built-in Dantec software) to the measured voltages to suppress high-frequency noise.

3 Numerical Simulation Setup

Non-reacting flow through the *Hi-Pilot* burner was simulated using the large-eddy simulation (LES) (Pope 2000) solver rhoPimpleFoam, available through the open source framework OpenFOAM (Weller et al. 1998). The rhoPimpleFoam solves the Favre-filtered transport equations for unsteady, compressible, non-isothermal single-phase fluid flows using a combination of the PISO (Pressure Implicit with Splitting of Operator) and SIMPLE (Semi-Implicit Method for Pressure-Linked Equations) algorithms (Issa 1986; Patankar and Spalding 1972), known as PIMPLE. Three outer and two inner correctors were used to couple solution variables inside the PIMPLE loop. A compressible solver was chosen as peak flow velocity at the throat of the nozzle can have a Mach number in excess of $M=0.3$.

The computational grid (Ceschin 2021) was generated using the tool CFMesh (Juretic 2015) to mesh a geometry created in the open-source platform “SALOME” (Code and Salome-Meca. 2018). The grid contains 35 million cells, with spatial resolution ranging down to 43 μm within the burner’s internal geometry. The grid spans 22 and 11 nozzle exit diameters in the axial and radial directions, respectively. The wall-adapting local eddy-viscosity model (WALE, (Nicoud and Ducros 1999)) was employed to compute the sub-grid-scale (SGS) eddy viscosity. The time step was kept fixed at 5×10^{-8} s, corresponding to a maximum Courant number of 0.3 in the computational domain. The Crank-Nicolson time differentiation scheme was blended with implicit Euler (0.5 factor) to ensure stability throughout the simulation. A second-order linear reconstruction was employed for the spatial discretization and a Sweby limiter (Sweby 1984) was applied to preserve monotonicity in the solution fields.

A schematic of the computational domain used in this study is shown in Fig. 1b. The inlet boundary condition was imposed to match the mass flow rate of the condition measured experimentally. The exit boundary condition was based on total pressure at the outlet (atmosphere). Therefore, the velocity field can either enter the domain according to the normal velocity at the patch or exit with a zero gradient boundary condition. Finally, to mimic experimental conditions, the co-flow plate was modelled as a no-slip wall, similarly to the burner geometry. After an initial start-up transient time of 0.5 s, the simulation was run for additional 0.3 s to obtain converged statistics on turbulent flow quantities.

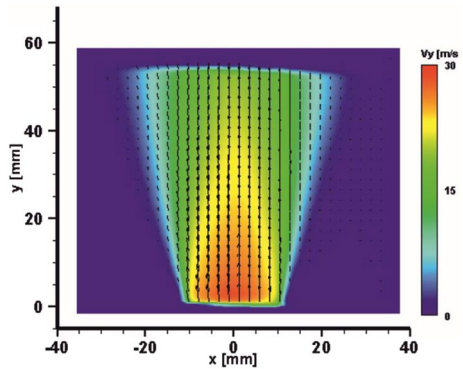
4 Results and Discussion

Although the mean and fluctuating velocity fields of the *Hi-Pilot* burner have been presented previously (Skiba et al. 2018, 2021; Wabel et al. 2017, 2018), the goal of this study is to understand the underlying mechanism responsible for its turbulent flow characteristics. As such, is it useful to begin with a complete description of the flow to confirm that the experimental conditions accurately replicate those reported previously.

4.1 Mean and Fluctuating Velocity Fields

Figure 2 shows the mean axial velocity field, as measured by the *wide-field* PIV system. As expected, one observes a high velocity core flow near the jet exit, which decreases in strength as the jet width grows with downstream distance. We note here that, in contrast

Fig. 2 Mean Axial Velocity



with the reacting flow cases described in the literature, no pilot flow was used in this study and therefore the mean axial velocity goes to zero at the periphery of the jet. Our decision to forgo the use of a co-flow was based on the fact that it would be impossible to replicate the density and viscosity ratio of the reacting flow test case in the non-reacting conditions. The use of a co-flow whose density is identical to that of the main flow would have a stabilizing effect on the shear-layer and thereby possibly affect the flow dynamics. To avoid this, we chose not to use a pilot flow in this study.

Figure 3 shows the fields of fluctuating axial (left) and radial (right) velocity computed from the measurements acquired with the wide-field PIV system. In the axial velocity fluctuations, we observe strong peaks at the periphery of the jet, which extend from the nozzle exit out to approximately 40 mm downstream. In the radial velocity fluctuations, we observe low fluctuation levels near the outer periphery of the flow near the nozzle, consistent with confinement by the nozzle wall. Radial velocity fluctuations at the jet periphery grow with downstream distance, consistent with the development of the shear-layers.

Figure 4 shows profiles of mean and fluctuating velocity at increasing downstream distance from the nozzle exit. In the left column are plotted the mean (in blue) and fluctuating (RMS, in red) components of axial velocity, as determined from the wide-field PIV measurements at 5, 25 and 50 mm downstream of the nozzle exit. In the right

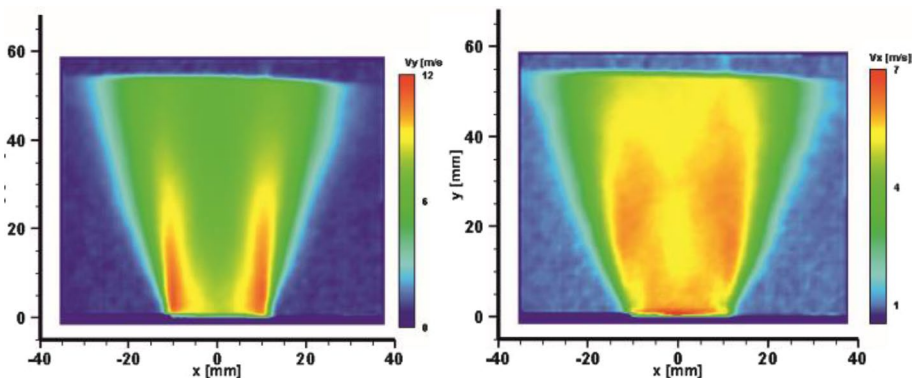


Fig. 3 Fluctuating axial (left) and radial (right) velocity fields

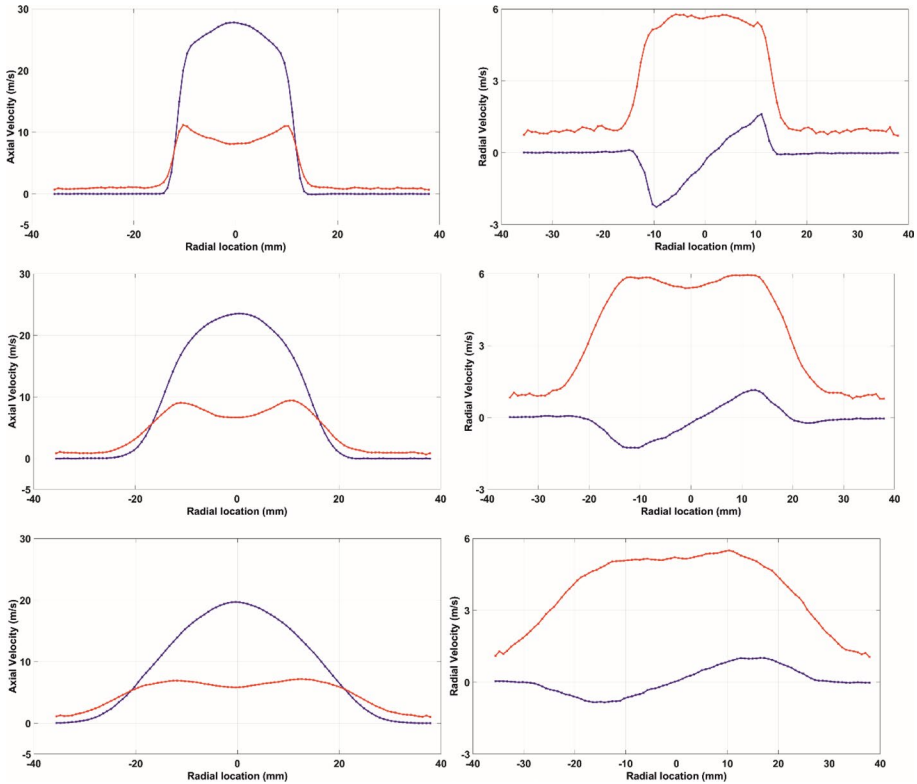


Fig. 4 Mean (blue) and StdDev (red) of axial (left) and radial (right) velocity, at $h=5$ mm (top), 25 mm (middle) and 50 mm (bottom)

column are similar profiles for the radial component of velocity. It is clear from this figure that the flow is symmetric about the jet centerline, both in the axial and radial component of velocity. As expected, the profiles of mean axial velocity peak at the jet centerline. In the profile closest to the nozzle exit (5 mm downstream), we observe $u'/U = 30\%$ at the jet centerline. This is consistent with values reported in the literature for this test case. The profiles of mean and fluctuating axial velocity are consistent with expected profiles for a jet of turbulent flow issuing into a quiescent environment.

The profiles of radial velocity fluctuations are more challenging to interpret. We observe that the radial velocity fluctuations appear uniform in magnitude across the width of the jet near the burner exit. The profile taken 25 mm downstream from the exit, however, shows a dual-peak profile, with maxima on either side of the axial centerline. The profile taken 50 mm from the burner exit is significantly wider, with a shape approaching that of a Gaussian distribution. Comparing these profiles with the corresponding data plotted in Fig. 3, we observe that this dual-peak structure in the radial velocity fluctuations persists from approximately 10 mm downstream of the burner exit to 40 mm, at which point the shear-layers at the periphery of the jet begin to merge at the centerline.

A plausible explanation for the change from a uniform distribution near the exit to a dual-peak profile further downstream is that the high velocity core of the jet is

oscillating or precessing within the nozzle. Upon exiting the nozzle, the oscillating core of the jet is confined within the axisymmetric (in the mean) shear-layer at the periphery of the jet. The profile of radial velocity fluctuations would then become dual-peaked as the core swivels back and forth within this region, before the shear-layers merge at the jet centerline.

4.2 Turbulence Isotropy

Figure 5 presents the probability density functions (PDFs) for axial and radial velocity fluctuations at the jet centerline at the same downstream locations of the velocity profiles shown in Fig. 4. In addition, the joint-PDFs (JPDFs) of axial vs. radial velocity fluctuations are presented. If the flow at the jet centerline were isotropic, one would expect symmetric profiles for each PDF and perfectly circular distributions for the JPDF of axial and radial fluctuations. Instead, we observe a more oval-shaped JPDF at each downstream location, with noticeably stronger fluctuations in the axial velocity than in the radial one. In addition, the PDFs of axial velocity fluctuations at the centerline show dual-peaked profiles at 5 and 50 mm downstream of the burner nozzle, and an asymmetric distribution profile at the intermediate location of 25 mm.

The lack of symmetry in PDFs of axial velocity fluctuations, together with more symmetric distribution of radial velocity fluctuations, is consistent with a low-frequency side-to-side oscillation or precession of the jet core around the burner axial centerline. Such oscillations would not necessarily induce large fluctuations in radial velocity. They would,

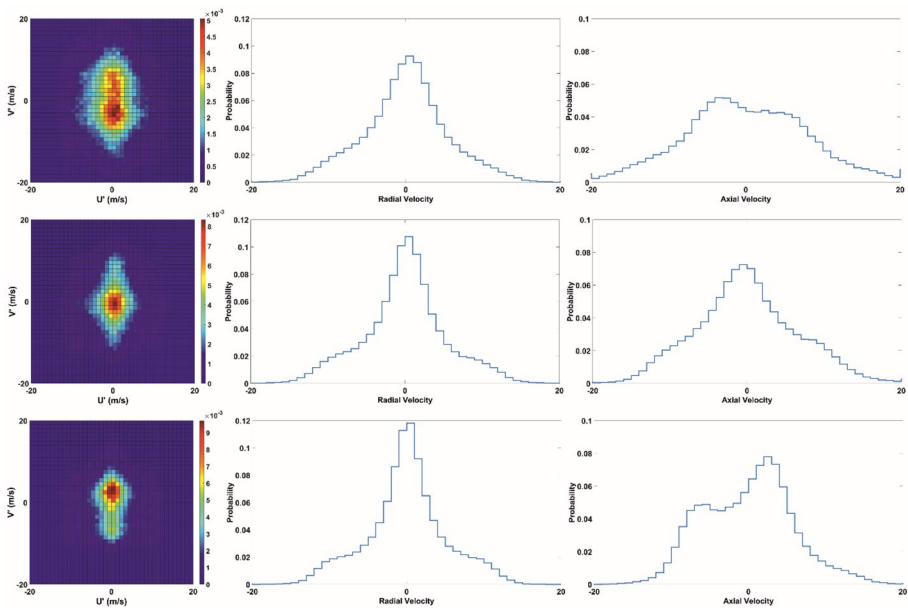


Fig. 5 JPFDs of radial vs axial velocity fluctuations taken on jet centerline at 5 mm (top), 25 mm (middle) and 50 mm (bottom) from the burner exit. Profiles in the middle and right columns represent PDFs of radial and axial velocity over the same region

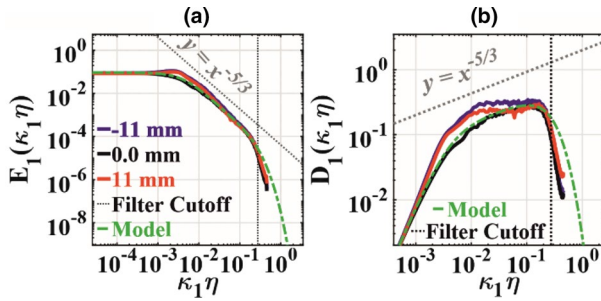


Fig. 6 One dimensional turbulent kinetic energy (E_1) and dissipation (D_1) spectra as a function of the spatial wavenumber (κ_1) normalized by the Kolmogorov length scale (η) in (a) and (b), respectively. The dashed green line represents Pope’s model spectra (Peters 1986) derived with a Taylor Reynolds number of 196. The dotted vertical line marks the 30 kHz cutoff frequency of the low pass filter applied to the hotwire measurements

however, result in large-scale fluctuations in perceived axial velocity as the high velocity core of the jet sweeps across the sampling location.

4.3 TKE Spectra

Figures 6a and b present, respectively, the one-dimensional (1-D) turbulent kinetic energy (TKE; $E_{1,1}$) and dissipation ($D_{1,1}$) spectra derived from hotwire measurements at the burner centerline ($x=0$) and near the jet periphery ($x = \pm 11$ mm). Here, $E_{1,1}$ and $D_{1,1}$ were derived in a manner similar to that in Refs. (McManus and Sutton 2020; Schmidt et al. 2021), with $E_{1,1} = \text{PSD}(V'')$ and $D_{1,1} = 2\nu_0\kappa_1E_1(\kappa_1\eta)$, where V'' represents the axial velocity fluctuations; PSD is the power-spectral density, ν_0 is the kinematic viscosity, κ_1 is the spatial wavenumber, and η is the Kolmogorov length scale (which is around 19 μm for the present case). Since hotwire measurements are temporal in nature, κ_1 was derived by invoking Taylor’s frozen-flow hypothesis and normalizing the temporal wavenumber associated with the measured spectra by the bulk flow velocity (~ 26 m/s for the present condition). The dashed green lines in Fig. 6 represent Pope’s (Pope 2000) 1-D model spectrum computed with a Taylor-scale-based Reynolds number of 196. Additionally, the 30 kHz cutoff frequency of the low-pass filter applied to the hotwire measurements is marked by the vertical dotted lines.

For the most part, the measured spectra in Fig. 6 show excellent agreement to that derived based on Pope’s theoretical model. This is particularly true within the inertial subrange; however, it is apparent that the smallest scales of the flow lie below that of the cutoff frequency and thus are not resolved by the present measurements. Nonetheless, it is evident from Fig. 6b that scales associated with the peak of the dissipation spectrum are well resolved.

We observe that the spectra computed at the jet periphery (i.e., at $x = \pm 11$ mm) exhibit a slight “bump” at large scales (i.e., where turbulent energy is put into the system). While those “bumps” represent a departure from the simplistic model proposed by Pope, it is evident that such spectra collapse to the same classical scaling at scales within and below the inertial subrange, where the predominant turbulent-flame interactions occur. Additionally, spectra derived within the central portion of the flow (e.g., $|x| < 9$ mm) are similar to that derived at the centerline (i.e., the solid black lines in Fig. 6) and do not display a “bump” at

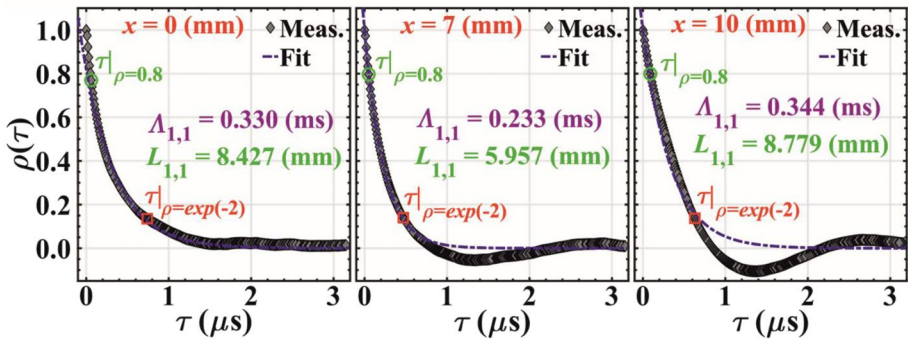
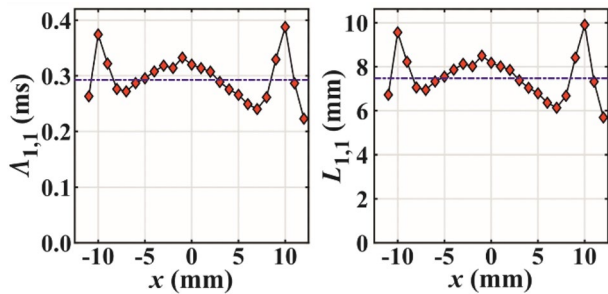


Fig. 7 Temporal Autocorrelations computed from HWA data

Fig. 8 Longitudinal integral timescale (left) and length scale (right) across the width of the reactant jet



the larger scales. In fact, it is clear from Fig. 6 that such spectra closely follow the modeled result at all scales.

The presence of this “bump” in the low-frequency region of TKE spectra computed at the jet periphery, together with its absence from the spectrum computed on the jet centerline, is consistent with the presence of a large-scale, relatively low-frequency oscillation or precession of the jet core within the expanding section of the burner nozzle. This oscillation needs not be at a single, sharp frequency to add considerable TKE to this region of the flow. Indeed, the “bump” observed in the TKE spectra is observable over approximately a half-decade on the frequency axis, i.e., over a relatively broad frequency range.

4.4 Longitudinal Integral Scales

Temporal autocorrelation of the hotwire velocity measurements was used to compute the longitudinal integral time scale ($\Lambda_{1,1}$) for the flow. Figure 7 shows the autocorrelations (ρ) as a function of lag-time (τ) from three radial locations: $x=0, 7,$ and 10 mm. Similar to the approach employed in Ref. (McManus 2019), here, the longitudinal integral time scales were derived by integrating under portions of the measured autocorrelation functions and applying exponential fits to them (i.e., dashed-blue lines in Fig. 7). Specifically, an exponential function of the form $c_1 \exp(c_2 \tau)$, with c_1 and c_2 being constants, were fit to the portions of the measured autocorrelation functions where their magnitudes resided between 0.8 and $\exp(-2) \approx 0.135$. These points are, respectively, referred to as $\tau|_{\rho=0.8}$ and $\tau|_{\rho=\exp(-2)}$ and are marked by the green circles and red squares in Fig. 7. After the fit was obtained, the

integral time scale was derived by integrating the measured autocorrelation from $\tau=0$ to $\tau|_{\rho=0.8}$ and adding that result to the integral of the fitted function from $\tau|_{\rho=0.8}$ to infinity. In this way, errors associated with poor convergence of ρ at large lags (Papageorge and Sutton 2016) are avoided, but the “Gaussian aspect” of ρ at small τ is retained (McManus 2019).

Using Taylor’s frozen-flow hypothesis, we multiplied the computed integral timescale by the bulk flow velocity of the jet and thereby determined the spatial integral length scale ($L_{1,1}$) to be 7.7 mm (marked by the horizontal dashed-blue line). Figure 8 shows the longitudinal integral time and length scales computed from the hot wire measurements across the entire width of the jet. We observe that the integral scale does not change significantly across the width of the jet. However, the values of $\Lambda_{1,1}$ and $L_{1,1}$ are observed to peak near the periphery of the jet (i.e., at $x = \pm 10$ mm).

4.5 Proper Orthogonal Decomposition

To better understand the turbulent flow characteristics, we performed a proper orthogonal decomposition (POD) on the PIV data. POD is a well-established technique in the field of fluid mechanics (Berkooz et al. 1993). The result of the POD is a set of orthogonal eigenmodes, representing coherent flow structures ordered by their contribution to the turbulent kinetic energy. For each eigenmode, temporal mode coefficients were obtained by taking the scalar products of the instantaneous flow-field with the eigenmode. We calculated the POD using the method of snapshots (Sirovich et al. 1987), based on 5000 frames of one PIV measurement run (i.e. every second frame).

Figure 9 shows the five most energetic eigenmodes computed from the PIV measurements. The plots in the upper and middle rows are colored according to the axial and radial components of velocity, respectively. The lower row shows vector representations of the velocity field vectors for each mode. Together these modes represent 27% of the TKE.

We observe that the first two eigenmodes show a dual-lobe structure in both the axial and radial velocity field components, consistent with the experimental values shown in Fig. 4. Modes 3 and 4 show a similar structure but with four lobes visible in the axial and

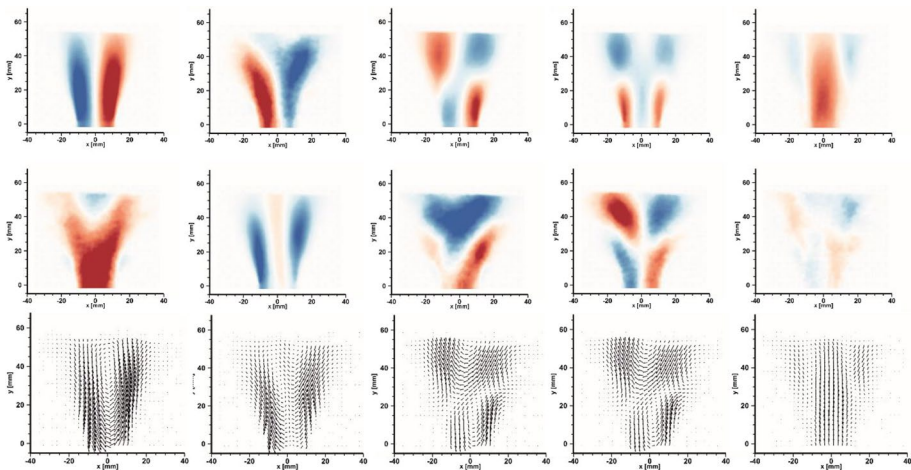


Fig. 9 First five eigenmodes of PIV data series. Color contours in the upper and middle rows denote axial and radial velocity, respectively. The lower row shows the vector structure

radial components of the velocity field. It is not until we get to the fifth eigenmode that we observe a significant flow structure along the axial centerline.

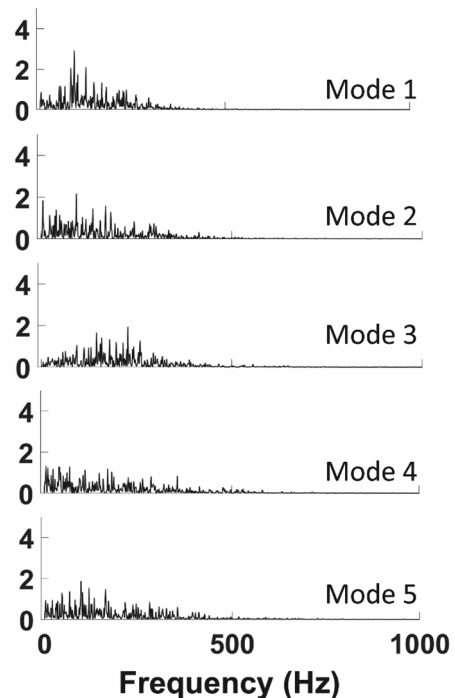
The spatial eigenmodes show that the majority of the TKE is to be found not on the jet centerline, but clustered along either side of it. Although some of this energetic content is certainly associated with the growth of the shear layer, the fact that these structures extend almost to the jet centerline at the nozzle exit indicates they also represent a large-scale oscillation of the jet core. Such an oscillation may result from a side-to-side oscillation or “flapping” of the jet core within the nozzle, or precession about the axial centerline.

Figure 10 shows the frequency spectra for the temporal mode coefficients of each of the five modes shown in Fig. 9. Each spectrum shows energy content spread over a broad (ca. 0–400 Hz) range of frequencies. The lack of a strong, narrow peak in the spectra indicates that the large-scale oscillations of the jet responsible for the dual-lobe structure of both velocity fluctuation fields and the spatial eigenmodes are broadband in nature, rather than coherent.

4.6 Sample PIV Measurement

Figure 11 shows a low-order reconstruction (based on the first five eigenmodes) of the PIV time-series measurements acquired with the wide-field PIV system. For clarity, only every tenth measurement of the series is shown, for a frame-to-frame time separation of 1 ms. The measurements included in this figure therefore correspond to the first 100 frames of the first measurement sequence. The color contour in this figure is based on the axial velocity.

Fig. 10 Frequency spectra of the time series of POD temporal modes



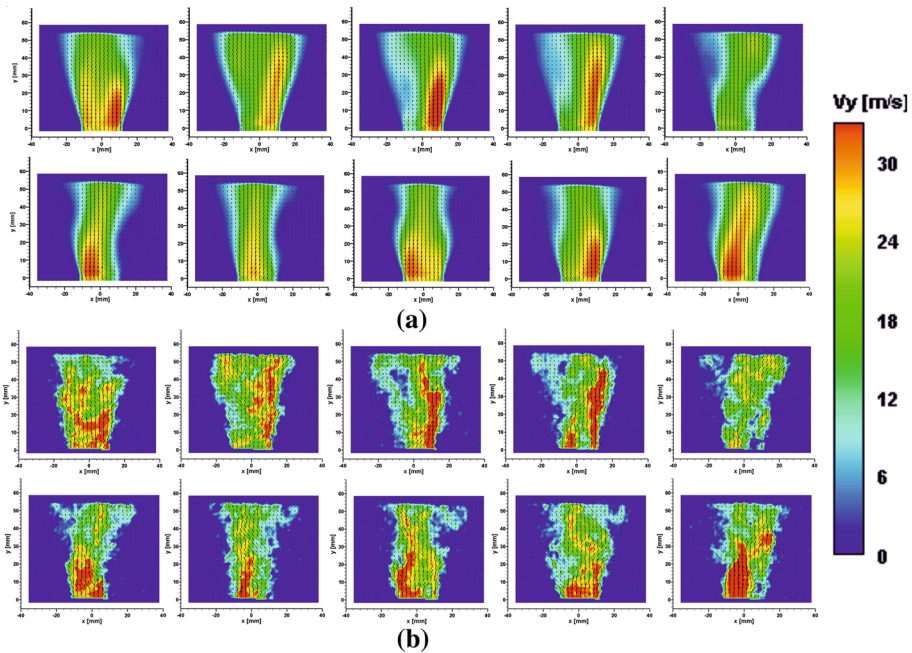


Fig. 11 **a** Reconstruction of PIV fields based on first five eigenmodes. **b** Initial vector fields upon which POD reconstruction is based. Every tenth frame displayed, for Δt of 1 ms

It is important to note here that the POD is a purely mathematic concept and care must be taken in the interpretation of results based thereon. The spatial eigenmodes computed via POD need not be associated with a specific fluid dynamic phenomenon such as the flapping or precession of a jet. The reconstruction below is based on the first 0.1% of the computed eigenmodes and represents 27% of the total TKE measured. It therefore highlights flow patterns with exceptionally high statistical significance. To demonstrate the POD reconstruction yields a realistic representation of the flow, the original vector fields upon which the reconstructed fields are based are also presented in Fig. 11.

In Fig. 11, we observe clear evidence of the jet-core sweeping past the axial centerline of the burner. In every frame, the instantaneous distribution of axial velocity is highly asymmetric, with a high velocity core to be found significantly to one side of the centerline or the other. In the first frame, we observe regions of high axial velocity on either side of the axis near the jet-exit. By the second frame of this sequence (i.e., 1 ms later) the high velocity region to the left of the centerline has disappeared, leaving a high velocity region only on the right side of the axis. This asymmetric distribution persists for approximately 2 ms, before sweeping over the left side of the axis. This time, however, the high-velocity core immediately begins to sweep back toward the right side of the centerline. The quasi-random side-to-side oscillation of jet core apparent in this measurement sequence is representative of the flow behavior observed throughout both PIV measurement acquisition runs.

The lack of optical access to flow upstream of the nozzle exit in this burner renders it impossible to experimentally confirm the fluid dynamic mechanism driving the observed side-to-side motion of the jet-core. Nevertheless, a reasonable hypothesis is that it results from flow-separation along the expanding section of the nozzle downstream of the

turbulence generator jets. Flow separation may be induced by either the unfavorable pressure gradient resulting from the expanding nozzle, or from the turbulence generator element (the slotted plate and transverse jets in the burner throat) leading to boundary layer separation in the nozzle. In either case, the result would be qualitatively the same. The partially separated boundary layer within the nozzle will lead to side-to-side forcing of the jet and thereby induce large-scale intermittency to the flow.

The POD analysis, together with the “bump” observed in the low-frequency region of the TKE spectra, indicate that large-scale oscillation of the high-velocity core of the jet around the axial centerline of the burner, possibly induced by boundary-layer separation in the burner nozzle, is a key mechanism responsible for the large (u', v') values measured in this burner. Large-scale, low-frequency intermittency may also be expected to bias the autocorrelation function toward timescales associated with this oscillation. Depending upon the frequency range of the large-scale intermittency, this may even lead to the computation of longitudinal integral scales that are larger than the exit diameter of the burner.

5 Numerical Simulations

As the experimental measurements are (inevitably) limited to the region downstream of the burner exit, we rely upon the LES computation for physical insight into the mechanism responsible for the oscillation/precession. Before we analyze these results, however,

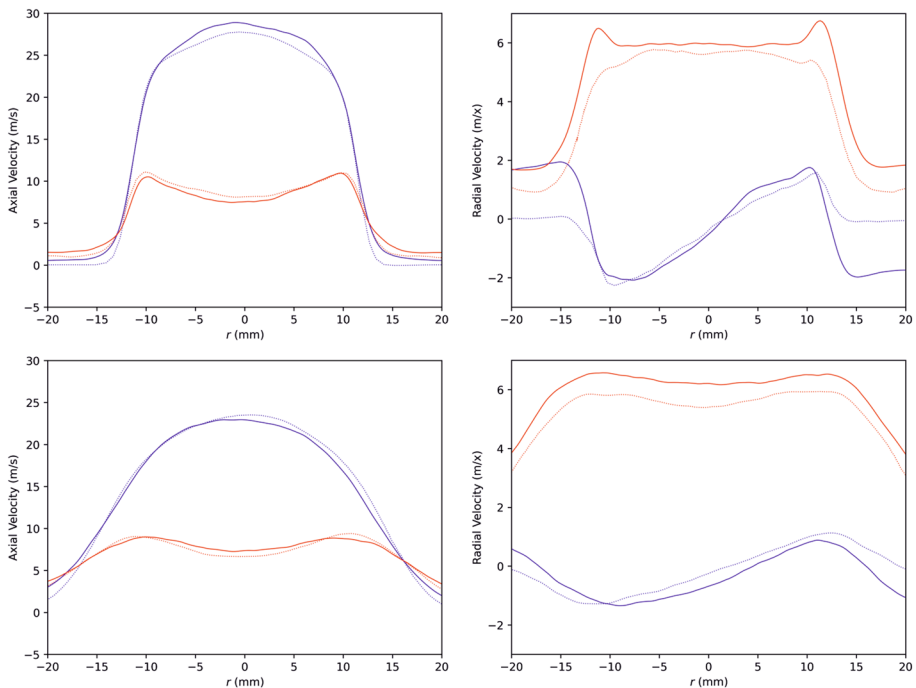


Fig. 12 Mean (blue) and StdDev (red) of Axial (left) and Radial (Right) velocity. Solid lines depict LES computation. Dotted Lines depict PIV measurements

it is necessary to confirm that the LES reliably captures the flow features observed in the experimental data. This comparison is presented below.

5.1 Mean and Fluctuating Velocity

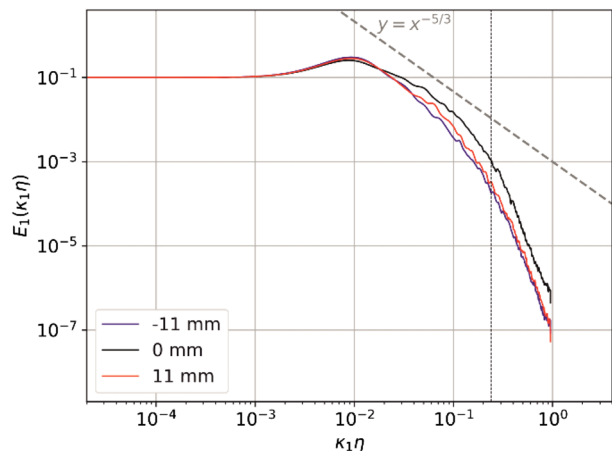
Figure 12 compares profiles of mean (blue) and fluctuating (red) velocity determined via experimental measurement and numerical simulation, at 5 and 25 mm downstream of the nozzle exit. In this figure, profiles for axial and radial velocity are shown in the left and right column, respectively. The profiles corresponding to the 5 and the 25 mm locations are at the top and bottom, respectively. The profiles show that both mean and fluctuating axial velocity profiles agree very well with the experimental data across the width of the jet. The profiles of mean radial velocity overlap well across the width of the jet but plateau at different values in the co-flow. This difference may stem from fact that in the PIV measurements, only air flow in the burner was seeded with particles, and therefore the entrainment of surrounding (unseeded) air is not well captured in the measurement.

We observe satisfactory agreement between measurement and simulations of radial velocity fluctuations across most of the width of the jet in Fig. 12. We note, however, that the LES predicts small peaks at the periphery of the jet, which are not observable in the profiles extracted from the PIV measurements. Similar peaks were observed in the profile of radial velocity fluctuations obtained via HWA. This may be a result of the lack of seeding of the ambient air leading to an under-prediction of radial velocity fluctuations. Although these peaks overlap in the shear-layer near the exit, they are spread over an area significantly larger than one would expect shear layer to be this close to the nozzle exit.

5.2 TKE Spectra

Figure 13 shows TKE spectra computed from the LES data at the same location and in the same manner as were done with the HWA data shown in Fig. 6. As one may expect,

Fig. 13 One dimensional turbulent kinetic energy (E_1) computed from the LES data



the spectra are not as well converged as those based on the HWA data. For example, the spectra computed at radial locations ± 11 mm do not overlap perfectly with that computed at the burner centerline. This is likely due to the shorter duration (0.2 s vs. 5 s for the HWA data) over which these TKE spectra were computed. The spectra for both data series are, however, consistent. Both show the same “bump” in the energy distribution at low wave numbers and approximately the same range over which the flow follows the $-5/3$ power law. This leads us to conclude that the LES is accurately reproducing the observed turbulent flow dynamics.

5.3 Spatial Eigenmodes

To compare the large-scale flow dynamics predicted via LES with those measured via PIV, we performed a POD on the axial velocity field data. Figure 14 shows the five most energetic eigenmodes computed from the velocity fields obtained via LES. Similar to those shown in Fig. 9, the plots in the upper and middle rows are colored according to the axial and radial components of velocity, respectively. The lower row shows vector representations of the velocity field vectors for each mode. Consistent with the eigenmodes computed from PIV data, the LES eigenmodes represent approximately 30% of the energy of the signal.

We observe that the first LES eigenmode, which accounts for approximately 11% of the TKE, closely resembles the same mode computed for the PIV data: it has a dual-lobe structure in both the axial and radial velocity fields that extends all the way to the burner

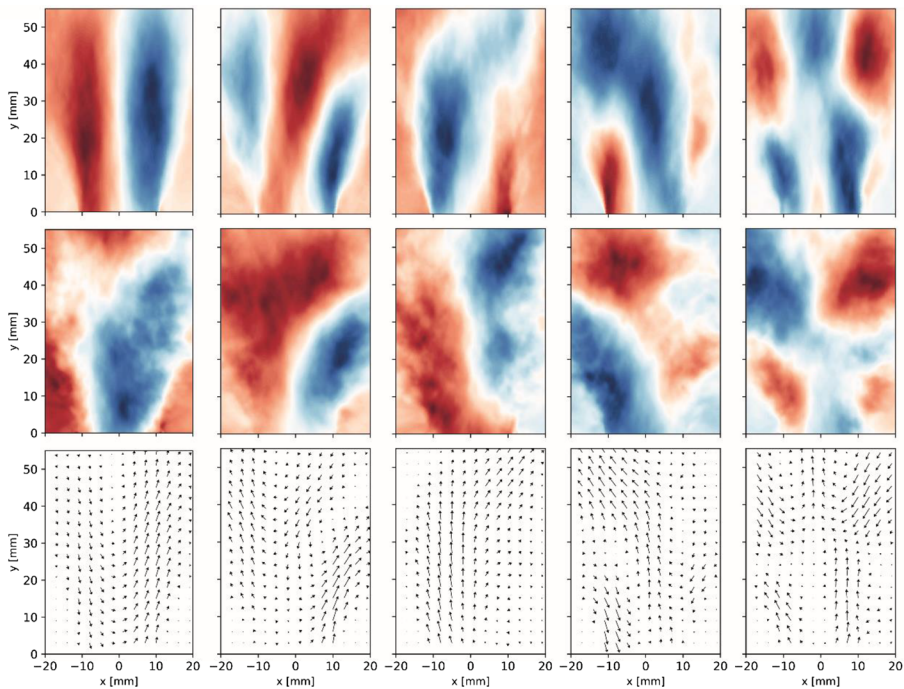


Fig. 14 First five eigenmodes of LES velocity field data. Color contours in the upper and middle rows denote axial and radial velocity, respectively. The lower row shows the vector structure

exit. Modes two through five do not show the same degree of similarity, possibly due to the shorter time over which the LES modes were computed compared to those of the PIV. What the eigenmodes tell us, however, is consistent with what we observe from the PIV measurements. The majority of the TKE is to be found not on the jet centerline, but clustered along either side of it. It is only in the fourth eigenmode that we observe more significant energetic content on the burner centerline than at the periphery of the jet. This, together with a lack of clear oscillation frequency observable in the temporal modes, indicates that a large scale, incoherent oscillation of the high velocity core of the jet accounts for most of the TKE.

5.4 Low-Order Reconstruction

Figure 15 shows a low-order reconstruction (based on the first five eigenmodes) of the axial velocity field data computed via LES. For direct, one-to-one comparison with the PIV data shown in Fig. 11, a frame-to-frame time separation of 1 ms is used.

Although the image sequences in Figs. 11 and 15 are clearly independent, the resemblance of their large-scale flow dynamics is remarkable. In Fig. 15, one observes a clear side-to-side oscillation of the high velocity core of the jet about the axial centerline of the burner. Just as in Fig. 11, this oscillation appears incoherent, without a clear frequency of oscillation. This, together with the clear similarity in the structure of spatial eigenmodes leads us to conclude the simulations are accurately replicating the large-scale jet oscillation phenomena observed in the measurements.

5.5 In-Nozzle Flow Separation

The data and analysis above show a large-scale oscillation of the high-velocity core of the jet about its mean axial centerline is a dominant feature of the turbulent flow field generated by the *Hi-Pilot* burner. This oscillation is likely associated with transient flow separation in

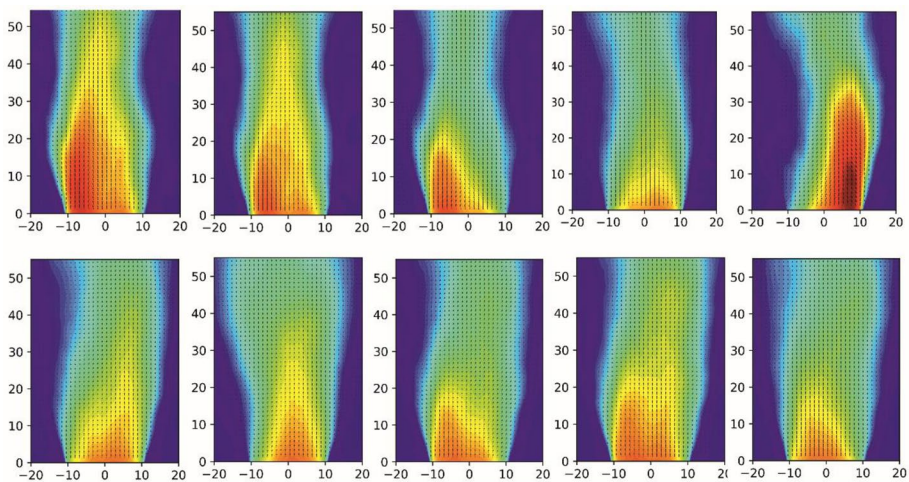


Fig. 15 Reconstruction of LES axial velocity fields based on first five eigenmodes. Frames are separated by 1 ms

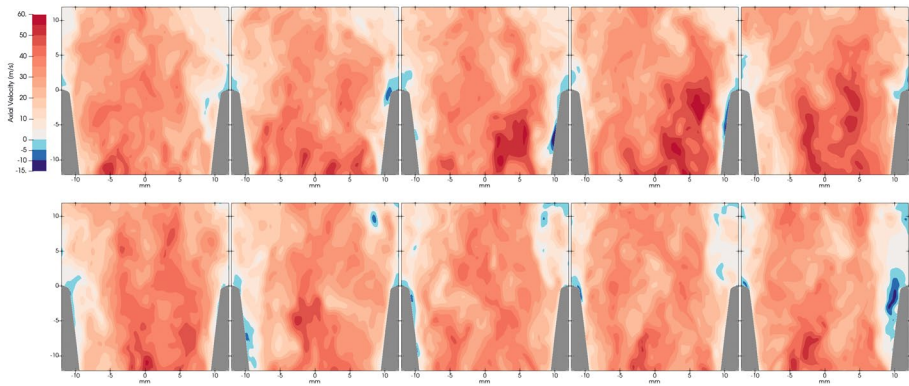


Fig. 16 Time of axial velocity data acquired in the Hi Pilot Nozzle, near the burner exit. Flow with positive velocity is shown in red, and negative in blue. Negative axial velocity of at the wall is indicative of flow separation there

the boundary layer at the wall of the expanding section of the reactant nozzle. The lack of optical access upstream of the nozzle exit, however, renders PIV measurement there impossible. As the LES data have been shown to accurately capture both the mean and fluctuating flow velocities downstream of the nozzle exit, as well as the large-scale flow dynamics, TKE spectra and integral length scale of the flow, it is reasonable to assume that if flow separation is present in the nozzle, it will be reliably captured in the LES data.

Figure 16 shows a time series of axial velocity within the nozzle, close to the burner exit. Flow with positive axial velocity is shaded red, and that with negative axial velocity is shaded blue. Each frame is separated in time by $200 \mu\text{s}$. In this figure, one observes clear evidence of flow separation (in the form of flow by the wall with negative axial velocity) within the nozzle, up to 10 mm upstream of the burner exit. The regions of reverse flow, which indicate separation, are highly transient and asymmetric, occurring mostly on either the left or the right side of the nozzle in any given frame. This is consistent with transient flow separation in a diffuser, which results in a large-scale oscillation of the high velocity core of the jet.

The last frame in Fig. 16 is particularly interesting, as it shows a relatively large region of strong ($> 10 \text{ m/s}$) reverse flow along the right side of the nozzle and past the rim of the burner exit. Indeed, the region of reverse flow extends far enough beyond the exit of the burner to enable transport of co-flow gases into the nozzle, and to transport them upstream of the exit. Although the region of reverse flow extends only a few ($\approx 2\text{--}3$) millimeters from the nozzle wall, the region of stagnant and low velocity ($< 10 \text{ m/s}$) extends 5–6 mm from the wall. As a result, the high velocity core of the jet is clearly deflected toward the left side of the nozzle. This deflection of the high velocity core of the jet opposite a region strong flow recirculation is consistent with the strong radial deflection of the jet core observable in Frame 3 of Fig. 11 and Frame 5 of Fig. 15.

The determination of whether the flow separation is the cause, or an effect of the jet oscillation, is beyond the scope of this study. Both the measurements and simulations indicate that large-scale, broadband oscillation of the jet core about its axial centerline are an important feature of the turbulent flow exiting *Hi-Pilot* nozzle. The computed axial velocity data presented in Fig. 16 shows clear evidence of flow separation within the nozzle. The final frame of Fig. 16 strongly suggests the two phenomena are coupled.

6 Conclusion

The *Hi-Pilot* burner is a widely used test case for the study of premixed flames subjected to high-intensity turbulence. With an innovative turbulence generation system consisting of a radially slotted plate and a converging–diverging nozzle with turbulence generator jets at the throat, flames with high Reynolds- and Karlovitz numbers ($> 99,000$ and 415 , respectively) have been studied in this piloted, premixed Bunsen burner. In this work we have applied experimental and computational tools to identify and characterize the mechanism or mechanisms by which these high turbulence intensities are achieved.

Large-scale oscillation of the high-velocity jet core about its own mean axial centerline is identified as an important feature of the turbulent flow field produced by this burner. The data shows this oscillation is linked to unsteady flow separation along the expanding section of the reactant nozzle. Particle image velocimetry (PIV), hot-wire anemometry (HWA) and high-fidelity, large-eddy simulation (LES) confirm the presence of large-scale, incoherent oscillation or “flapping” of the jet-core downstream of the burner exit. Consistent with previous studies in this burner, significant anisotropy is observed in the radial and axial velocity fluctuations. Proper orthogonal decomposition (POD) of both the measured and the computed velocity field data confirm this anisotropy results primarily from a large scale, low-frequency (ca. $100\text{--}300$ Hz) oscillation of the jet core around the burner centerline. While this oscillation appears stochastic in nature, it occurs at frequencies below where the TKE spectra begins to follow a $-5/3$ power law, resulting in flow intermittency and a separation of scales in the turbulent flow. Analysis of the LES data confirms the presence of transient flow separation within the nozzle of the burner and shows it to be linked to the large-scale oscillation.

In conclusion, we find that the turbulent flow field of the *Hi-Pilot* burner represents high-intensity turbulence driven in large part by oscillation of a high velocity jet about the axial centerline of the burner. This oscillation results from flow-separation in the nozzle and results in a flow at the exit with significant scale separation in the TKE spectra. Although scale separation and intermittency are not unusual in turbulent flows, we note that in-nozzle flow separation is highly sensitive to both bulk-flow velocity and upstream turbulence characteristics. This insight should inform analysis, interpretation and modeling of earlier and future studies of this unique test case.

Supplementary Information The online version contains supplementary material available at <https://doi.org/10.1007/s10494-022-00328-8>.

Acknowledgements This project has received funding from the European Research Council (ERC) under the European Union’s Horizon 2020 research and innovation programme (Grant agreement No.682383). AC, FEHP and HGI acknowledge the support of King Abdullah University of Science and Technology (KAUST) and computational resources provided by the KAUST Supercomputing Laboratory (KSL).

Funding Open Access funding enabled and organized by Projekt DEAL.

Declarations

Ethical approval The authors declare they have no conflicts of interest, financial or non-financial.

Open Access This article is licensed under a Creative Commons Attribution 4.0 International License, which permits use, sharing, adaptation, distribution and reproduction in any medium or format, as long as you give appropriate credit to the original author(s) and the source, provide a link to the Creative Commons licence, and indicate if changes were made. The images or other third party material in this article

are included in the article's Creative Commons licence, unless indicated otherwise in a credit line to the material. If material is not included in the article's Creative Commons licence and your intended use is not permitted by statutory regulation or exceeds the permitted use, you will need to obtain permission directly from the copyright holder. To view a copy of this licence, visit <http://creativecommons.org/licenses/by/4.0/>.

References

- Berkooz, G., Holmes, P., Lumley, J.L.: The proper orthogonal decomposition in the analysis of turbulent flows. *Ann. Rev. Fluid Mech.* **25**, 539–575 (1993)
- Ceschin A., Angelilli, L., Hernández Pérez, F.E., Boxx, I., Im. H.G.: Study on coherent structures for high turbulence burner. 59th AIAA Aerospace Sciences Meeting (virtual). AIAA 2021–1849. (2021). <https://doi.org/10.2514/6.2021-1849>
- Aster Code. Salome-Meca. (2018)
- Driscoll, J.F.: Turbulent premixed combustion: flamelet structure and its effect on turbulent burning velocities. *Prog. Energy Combust. Sci.* **34**, 91–134 (2008)
- Driscoll, J.F., Chen, J.H., Skiba, A.W., Carter, C.D., Hawkes, E.R., Wang, H.: Premixed flames subjected to extreme turbulence: some questions and recent answers. *Prog Energy Combust. Sci.* **76**, 100802 (2020)
- Fox, R.W., Kline, S.J.: Flow regimes in curved subsonic diffusers. *J. Basic Eng.* **84**, 303–312 (1962)
- Griebel, P., Siewert, P., Jansohn, P.: Flame characteristics of turbulent lean premixed methane/air flames at high pressure: Turbulent flame speed and flame brush thickness. *Proc. Combust. Inst.* **31**, 3083–3090 (2007)
- Hurst, D., Vassilicos, J.C.: Scalings and decay of fractal-generated turbulence. *Phys. Fluids* **19**, 035103 (2007)
- Issa, R.I.: Solution of the implicitly discretised fluid flow equations by operator-splitting. *J. Comput. Phys.* **62**(1), 40–65 (1986)
- Janicka, J., Sadiki, A.: Large eddy simulation of turbulent combustion systems. *Proc. Combust. Inst.* **30**, 537–547 (2005)
- Juretic, F.: “cfMesh User Guide”. In: Creative Fields, Ltd 1 (2015)
- Li, Z., Li, B., Sun, Z., Bai, X.-S., Aldén, M.: Visualization of multi-regime turbulent combustion in swirl-stabilized lean premixed flames. *Combust Flame* **157**, 1087–1096 (2014)
- Marshall, A., Venkateswaran, P., Noble, D., Seitzman, J., Liewuven, T.: Development and characterization of a variable turbulence generation system. *Exp Fluids* **51**, 611–620 (2011)
- McManus T. A.: An Experimental Investigation of the Relationship between Flow Turbulence and Temperature Fields in Turbulent Non-premixed Jet Flames, Ph.D. thesis (2019)
- McManus, T.A., Sutton, J.A.: Simultaneous 2D filtered Rayleigh scattering thermometry and stereoscopic particle image velocimetry measurements in turbulent non-premixed flames. *Exp. Fluids* **61**(6), 134 (2020)
- Nicoud F. and Ducros F.: “Subgrid-scale stress modelling based on the square of the velocity gradient tensor”. In: *Flow, Turbulence and Combustion* 62.3, pp. 183–200 (1999)
- Papageorge, M., Sutton, J.A.: Statistical processing and convergence of finite-record-length time-series measurements from turbulent flows the proper orthogonal decomposition in the analysis of turbulent flows. *Exp. Fluids* **57**, 126 (2016)
- Patankar, S.V., Spalding, D.B.: A calculation procedure for heat, mass and momentum transfer in three-dimensional parabolic flows. *Int. J. Heat Mass Transf.* **15**(10), 1787–1806 (1972)
- Peters, N.: Laminar flamelet concepts in turbulent combustion. *Proc. Combust. Inst.* **21**, 1231–1250 (1986)
- Peters, N.: *Turbulent combustion*. Cambridge University Press, Cambridge (2000)
- Pope, S.B.: *Turbulent flows*. Cambridge University Press, Cambridge (2000)
- Roach, P.E.: The generation of nearly isotropic turbulence by means of grids. *Int. J. Heat Fluid Flow* **8**, 82–92 (1986)
- Schmidt, B.E., Skiba, A.W., Hammack, S.D., Carter, C.D., Sutton, J.A.: Combustion in the future: the importance of chemistry. *Proc. Combust. Inst.* **38**, 1–9 (2021)
- Sirovich, L.: Turbulence and the dynamics of coherent structures I. coherent structures. *Q. Appl. Math.* **45**(3), 561–571 (1987)
- Skiba, A.W., Wabel, T.M., Carter, C.D., Hammack, S.D., Temme, J.E., Driscoll, J.F.: Premixed flames subjected to extreme levels of turbulence part I: flame structure and a new measured regime diagram. *Combust. Flame* **189**, 407–432 (2018)

- Skiba, A.W., Hammack, S.D., Carter, C.D., Driscoll, J.F.: Premixed flames subjected to extreme levels of turbulence part II: Surface characteristics and scalar dissipation rates. *Combust Flame* **111**, 1703 (2021)
- Sweby, P.K.: High resolution schemes using flux limiters for hyperbolic conservation laws. *SIAM J. Numer. Anal.* **21**(5), 995–1011 (1984)
- Venkateswaran, P., Marshal, A., Shin, D.H., Noble, D., Seitzman, J., Lieuwen, T.: Measurements and analysis of turbulent consumption speeds of H₂/CO mixtures. *Combust Flame* **158**, 1602–1614 (2011)
- Venkateswaran, P., Marshall, A.D., Seitzman, J.M., Lieuwen, T.C.: Turbulent consumption speeds of high hydrogen content fuels from 1–10 atm. *J. Eng Gas Turb Power.* **136**, 011504–1 (2014)
- Wabel, T.M., Skiba, A.W., Temme, J.E., Driscoll, J.F.: Measurements to determine the regimes of premixed flames in extreme turbulence. *Proc. Combust. Inst.* **36**, 1809–1816 (2017)
- Wabel, T.M., Skiba, A.W., Driscoll, J.F.: Evolution of turbulence through a broadened preheat zone in a premixed piloted Bunsen flame from conditionally-averaged velocity measurements. *Combust. Flame* **188**, 13–27 (2018)
- Wang, Z., Zhou, B., Yu, S., Brackmann, C., Li, Z., Richter, M., Alden, M., Bai, X.-S.: Structure and burning velocity of turbulent premixed methane/air jet flames in thin-reaction zone and distributed reaction zone regimes. *Proc. Combust. Inst.* **37**, 2537–2544 (2019)
- Weller, H.G., Tabor, G., Jasak, H., Fureby, C.: A tensorial approach to computational continuum mechanics using object-oriented techniques. *Comput. Phys.* **12**, 620–631 (1998)
- White, F.M.: *Fluid mechanics*, 4th edn. McGraw-Hill, New York (1998)
- Zhou, B., Costa, M., Li, Z., Alden, M., Bai, X.-S.: Characterization of the reaction zone structures in a laboratory combustor using optical diagnostics: from flame to flameless combustion. *Proc. Combust. Inst.* **36**, 4305–4312 (2017a)
- Zhou, B., Brackmann, C., Li, Z., Aldén, M., Bai, X.-S.: Simultaneous multi-species and temperature visualization of premixed flames in the distributed reaction zone regime. *Proc. Combust Inst.* **35**, 1409–1416 (2014)
- Zhou, B., Brackmann, C., Li, Q., Wang, Z., Petersson, P., Li, Z., Aldén, M., Bai, X.-S.: Distributed reactions in highly turbulent premixed methane/air flames. *Combust Flame* **162**, 2937–2953 (2015a)
- Zhou, B., Li, Q., He, Y., Petersson, P., Li, Z., Aldén, M., Bai, X.-S.: Visualization of multi-regime turbulent combustion in swirl-stabilized lean premixed flames. *Combust Flame* **162**, 2954–2958 (2015b)
- Zhou, B., Brackmann, C., Wang, Z., Li, Q., Richter, M., Aldén, M., Bai, X.-S.: Thin reaction zone and distributed reaction zone regimes in turbulent premixed methane/air flames: scalar distributions and correlations. *Combust Flame* **175**, 220–236 (2017b)